



OPEN

Magnetic single atom catalyst in C₂N to induce adsorption selectivity toward oxidizing gases

Muhammad Mushtaq^{1,2} & Nacir Tit^{1,2}✉

Density functional theory (DFT) method is used to study the effect of single-atom catalyst (SAC) of Mn embedded in C₂N nanoribbon (C₂N-NR) on the adsorption properties as an attempt to achieve selectivity. Many gases (e.g., CO, CO₂, H₂, H₂O, H₂S, N₂ and O₂) of interest to energy and environmental applications were tested. The results show that SAC-Mn alters chemisorption processes with all gas molecules except N₂. Clear adsorption selectivity is obtained towards oxidizing CO, CO₂ and O₂ molecules as evidenced by the enhancements in binding energy and charge transfer and the reduction in magnetization. While the SAC-Mn contributes predominantly to Fermi-energy region with spin-down states, the strong binding to oxidizing molecules introduces there more spin-up states to compromise and reduce the magnetization. Hence, C₂N-NR:Mn is proposed to be used as platform for gas sensor (if combined with magnetic sensor) to yield high selectivity toward these latter gases.

The discovery of graphene by Geim and Novoselov¹ has opened an immense field of 2D systems with promising high-tech applications rich with excitement and discoveries and has effectively boosted the technology toward the fabrication of nano-devices². Actually, soon after the Nobel prize ceremony in 2010, very fast development has been taking place and the dream of the inventors is getting realized day after day. Graphene becomes a special and a unique material known with its great flexibility and multi-functionality. For instance: (i) In gas-sensing: The inventors anticipated graphene to take the lead to have an extraordinary sensitivity to the limit of detecting individual gas molecules³. Indeed, room temperature detections of many gases, which used to be challenging tasks using metal-oxides (e.g., SnO₂ and ZnO), became achievable using graphene and related 2D materials with high sensitivity at order of ppb and thus reaching outstanding selectivity^{4,5}. (ii) In nano-electronics: It was considered for post-silicon nano-electronics such as graphene-based field-effect transistor (G-FET)^{6,7}. (iii) In photonics: The functionalization of graphene induced energy gap in it and made it rather concurrent for diversity of photonic applications ranging from dye-sensitized solar cells to LED to touch screens to photodetectors and to ultrafast lasers^{8–13}. (iv) In spintronics: Even though with the apparent lack of magnetism and the weak of spin-orbit coupling, magnetic impurities in graphene find unusual host for their spin relaxation to promote graphene to become distinct material for spin transport and spintronic devices^{14,15}. (v) In biomedicine: Graphene finds broad field of applications ranging from drug delivery to cancer therapies to bio-sensing (i.e., to detect glucose, dopamine, protein and DNA)^{16,17}. (vi) In strain sensors: Functionalization of graphene (e.g., graphene oxide) can reduce its stiffness to become suitable for strain sensing^{18,19}.

Another more recent breakthrough was achieved in 2015 by the successful synthesis of new material based on the nitrogenated holey graphene “C₂N” by Mahmood and co-workers using a bottom-up wet chemical reaction method²⁰. C₂N not only has a uniform distribution of holes but each hole is bordered with aromatic nitrogen atoms to widen the energy gap between the valence and conduction bands and, consequently, making itself useful for semiconducting applications (i.e., E_g ≈ 1.90 eV)²⁰. This novel material has been proven to be very thermodynamically stable and having a large uptake capacity to adapt embedding metal catalysts in its holes that can trigger either high selectivity toward toxic gases at room temperature (e.g., in case of using transition metal catalyst) or enhanced uptake capacity in case of metal-ion battery (MIB) applications (e.g., in using light metal atoms like: Li, Na, K, Ca)^{21–25}. Furthermore, the downsizing of these metal nanostructures to singly-dispersive metal atoms would be highly desirable for maximizing the efficiency of catalytically active metal site^{26–28}. The single-atom catalyst (SAC) and double-atom catalyst (DAC) nanostructures have been experimentally achieved in metal oxides and in C₂N and shown very enhanced catalytic activity towards several toxic gas reduction

¹Department of Physics, College of Science, UAE University, P.O. Box 15551, Al-Ain, United Arab Emirates. ²National Water and Energy Center, UAE University, P.O. Box 15551, Al-Ain, United Arab Emirates. ✉email: ntit@uaeu.ac.ae

reactions (e.g., CO_x, NO_x and SO_x) of environmental concern^{29–31}. The successful syntheses of SAC and DAC in C₂N also inspired and triggered many theoretical efforts to study the corresponding reaction mechanisms^{32–34}.

On the computational side, many researchers reported the importance of utilization of transition metal (TM) atoms as catalysts for gas-sensing applications. For instance, Zhao and co-workers reported DFT results of the effect of copper dimer (Cu₂) embedded in C₂N on the reduction of CO₂ to hydrocarbons³⁵. Ma and co-workers used DFT to test the embedment of five TM atoms (i.e., Sc, Ti, V, Cr and Mn) in C₂N for CO and O₂ oxidation reactions. They concluded that the best catalyst among these to be Cr and Mn³⁶. In a related work, Liu and co-workers presented a combination of electrochemical measurements and DFT calculations to study and compare the catalytic activity of MnN₄ to FeN₄ embedded in graphene in inducing the oxygen reduction reaction (ORR). They clearly demonstrated the superiority of MnN₄ catalyst³⁷. In a different study based on DFT, Impeng and co-workers investigated the correlation between magnetic moment and strength of chemisorption of 13 gases on MnN₄-embedded graphene³⁸. Only five gases (i.e., NO, NO₂, O₂, CO, and SO₂) exhibited strong chemisorption with large binding energies (-2.30, -1.42, -1.32, -1.11, and -0.51 eV, respectively). Furthermore, only three gases (i.e., NO, CO and NO₂) were able to reduce the magnetization from 3.01 μ_B to 0.13, 1.04, and 2.01 μ_B, respectively. The estimated recovery times for these three gases were large except CO gas to have 1.7 s. So, the authors proposed MnN₄-embedded graphene as a platform for a promising magnetic sensor for CO detection³⁸. Regarding the magnetism of TM-atom embedded in C₂N, Du and co-workers presented DFT study of magnetization due to the embedment of 3d-TM atoms into the pore of C₂N. They reported the existence of ferromagnetic ground state for TM atoms: Sc, Ti, V, Cr, Mn, Fe, Co and Ni, and paramagnetic state for Cu and Zn³⁹. Wang and co-workers presented DFT study of magnetization in C₂N nanoribbons (C₂N-NRs) under the effect of diversifying the passivation of the dangling bonds of the edge atoms⁴⁰. They reported that armchair-edged C₂N-NR is a non-magnetic semiconductor with direct gap. Whereas zigzag-edged C₂N-NR is magnetic either semiconductor with indirect band-gap or metallic. Besides the co-saturation of edges with (H and O) or (F and O) can induce a large magnetization into the system to make the system an interesting material for spintronic devices⁴⁰.

The scope of the present work is to study the effect of a magnetic SAC-Mn embedded in C₂N nanoribbon on the adsorption of seven gases of energy and environmental interest (e.g., CO, CO₂, H₂, H₂O, H₂S, N₂ and O₂) using the state-of-the-art DFT based on VASP. The aim is the attainment of selectivity and analyzing the reasons behind it or its origins, with hypothesis to include among the arguments the inspection of variation of magnetization and charge transfer (i.e., type of molecule whether oxidizing or reducing). The paper is organized as follows: Last section gives details about the model and the computational method. Section 2 gives elaboration of discussing the results. The concluding section summarizes our main findings.

Results and discussion

Atomic relaxations. As first stage, the adsorptions of gas molecules on pristine C₂N nanoribbons were attempted. Atomic relaxations of gas molecules (e.g., CO, CO₂, H₂, H₂O, H₂S, N₂ and O₂) were included in our study. All molecules are found to exhibit physisorption processes on pristine C₂N-NR and prefer to stabilize above the main pore of the C₂N-NR at a height of about 2.12, 2.39, 1.61, 1.25, 1.42, 2.30, and 2.0 Å, respectively. In case of angular molecules (e.g., H₂O and H₂S) the reported distances are even lower (1.25 and 1.42 Å, respectively) as these molecules are found to stabilize by having their arms directed toward the surface; as likely due to H atoms being electropositive and getting attracted to the electronegative nitrogen atoms of the pore via van der Waals interactions. In the physisorption states of these latter 2 molecules, their angles are found decreased to 101° and 90°; while in the cases of free molecules the angles used to be about 104° and 92°, respectively. Such reductions in angular parameters might be attributed to the transfer of charge from surface to molecules; especially as being oxidizing molecules. However, for the other linear molecules (CO, CO₂, H₂, N₂, O₂), they seem to stabilize at distances more than 2.0 Å above the surface and in horizontal position parallel to the surface with molecular atoms being close to N-atoms along the direction of the diagonal of the pore.

In second stage, the adsorptions of the same gas molecules were attempted on Mn-embedded C₂N-NRs (i.e., C₂N-NR:Mn). The results of atomic relaxations are shown in Fig. 1. Chemisorption processes seem to be the destiny to occur for all molecules except N₂, whose triplet covalent bond seems strong and not dissociable to persist in yielding physisorption process. The N₂ molecule stabilizes at a distance 3.10 Å above Mn-atom. Table 1 shows the adsorption energy in case of N₂ to be as low as E_{ads} = -0.123 eV and the molecule to be oxidizing the Mn catalyst with mimic charge transfer of about -0.0178 e. The effect on magnetization is, in turn, very mimic of about 0.027 μ_B reduction to corroborate the weak interaction between N₂ molecule and Mn-catalyst.

All other studied molecules are found to act as oxidizing the Mn-catalyst. Three molecules (O₂, CO, and CO₂) seem to bond strongly to the Mn catalyst causing huge effect on its magnetization more than any other molecule, with reductions of about 1.011 μ_B, 0.303 μ_B and 0.913 μ_B, respectively. Also, the charge exchanges are drastically large of about -0.779 e, -0.173 e and -0.570 e, respectively. These two indications are signals of potential occurrence of selective gas-sensing of C₂N-NR:Mn towards these three molecules. It should be emphasized that the chemisorption of O₂ occurs with partial molecular dissociation as the molecule breaks its π-bond to pave the way for the two oxygen atoms to form new bonds with Mn-catalyst. In case of CO-molecule chemisorption, the bond is formed between Mn-C as carbon atom has ability for four valency. Again, in chemisorption of CO₂-molecule, the two π-bonds between C-O breaks to pave the way for C-atom to form covalent bond with Mn-catalyst. Consequently, the angle of CO₂ molecule changes from 180° to 144°.

Relatively weaker chemisorption processes of different style of bonding occur between H₂-based molecules and the Mn-catalyst embedded in the pore of C₂N-NR. Panels 1 (e–f) show the relaxed structures of H₂O and H₂S on C₂N:Mn-NRs. Mn-catalyst forms covalent bond with the anionic atom in the molecule with bond-length d(Mn–O) = 1.99 Å and d(Mn–S) = 2.44 Å. Specifically, the O-atom has stronger bond with Mn than does S-atom because it has more electronegativity (i.e., χ^O = 3.44 Pauling > χ^S = 2.58 Pauling). The hydrogen arms of

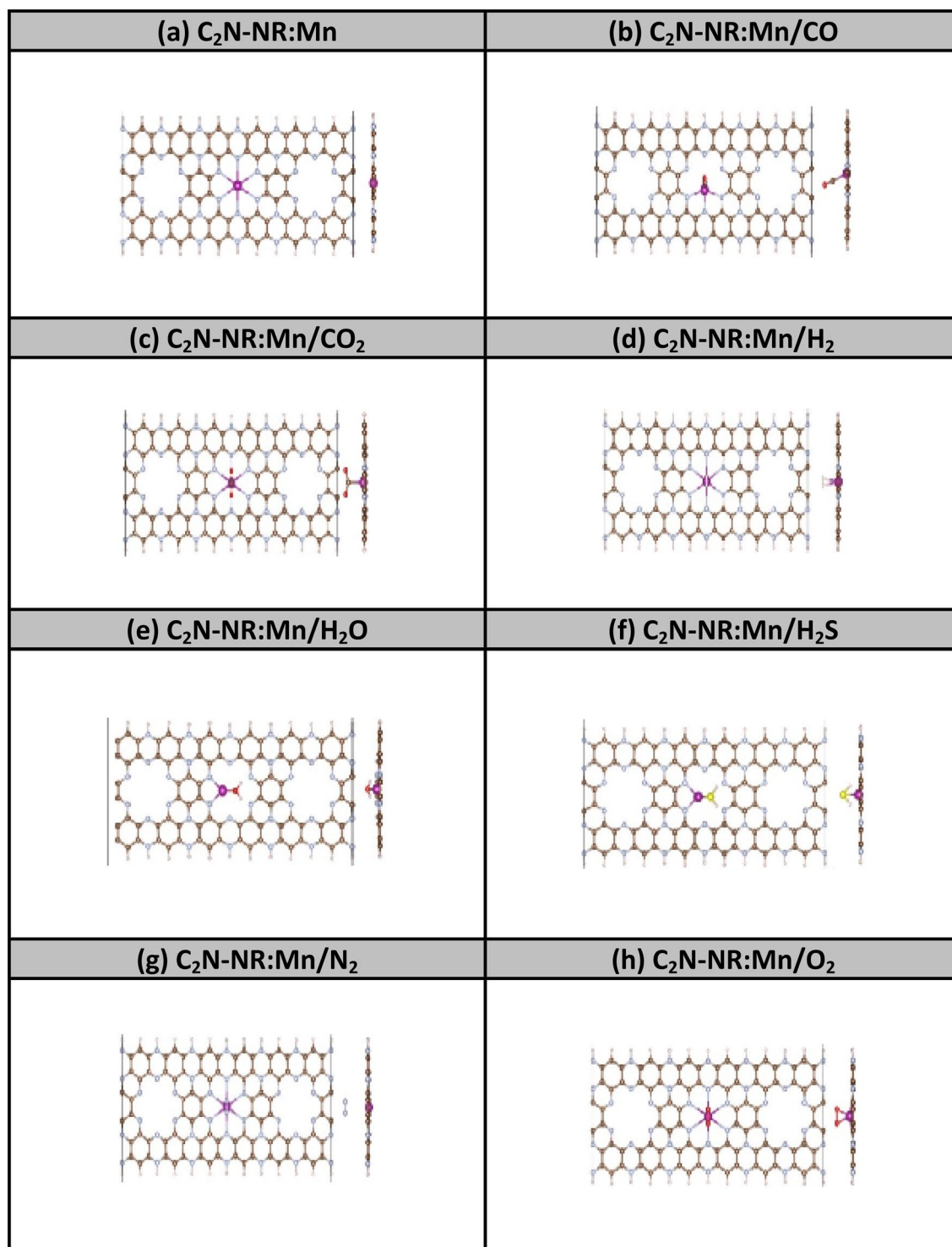


Figure 1. Relaxed geometries of C₂N-NR:Mn with various gas molecules. Colors: C (brown), N (blue), Mn (purple), O (red), H (yellow), S (orange), and N (grey).

molecules are directed closer to the surface as could be attributed to the molecular dipole interaction with the surface dipole moments. The effects of these two bonding structures on the charge transfer and magnetization are similar but smaller compared to the previous group of molecules (i.e., O₂, CO, CO₂). The chemisorption of H₂ molecule, shown in Panel 1(d), has similar mimic effects on Δq and ΔM and, thus, should belong to this group. The bond length $d(\text{H}-\text{H}) = 0.76 \text{ \AA}$ is a bit larger than the free molecule. The molecule looks like it did not split because the calculation is carried out at 0 K under the assumption of frozen-lattice and the validity of the Born–Oppenheimer approximations.

System	E_{ads} (eV)	Δq (e)	M (μ_B)	ΔM (μ_B)
C ₂ N-NR	N/A	N/A	0	0
C ₂ N-NR:Mn	N/A	N/A	4.868	0
C ₂ N-NR/CO	-0.244	-0.016	0	0
C ₂ N-NR:Mn/CO	-1.094	-0.173	4.565	-0.303
C ₂ N-NR/CO ₂	-0.296	-0.014	0	0
C ₂ N-NR:Mn/CO ₂	-0.985	-0.570	3.955	-0.913
C ₂ N-NR/H ₂	-0.093	+0.874	0	0
C ₂ N-NR:Mn/H ₂	-0.194	-0.002	4.833	-0.035
C ₂ N-NR/H ₂ O	-0.059	-0.015	0	0
C ₂ N-NR:Mn/H ₂ O	-0.188	-0.021	4.949	+0.081
C ₂ N-NR/H ₂ S	-0.083	-0.006	0	0
C ₂ N-NR:Mn/H ₂ S	-0.129	-0.016	4.967	+0.099
C ₂ N-NR/N ₂	-0.213	-0.014	0	0
C ₂ N-NR:Mn/N ₂	-0.123	-0.018	4.841	-0.027
C ₂ N-NR/O ₂	-0.118	-0.020	2.047	0
C ₂ N-NR:Mn/O ₂	-1.564	-0.779	3.587	-1.011

Table 1. Adsorption energetics (i.e., E_{ads} = adsorption energy) and magnetization of C₂N-NR and C₂N-NR:Mn before and after adsorption of gas molecules. Charge transfer ($\Delta q = q - q_0$), magnetization (M), and change of magnetization ($\Delta M = M - M_0$). All the samples are metallic.

Spin-polarized band-structures. Figure 2 displays the spin-polarized band structures of Mn-embedded in C₂N-NR and its interactions with the 7 studied molecules in same order as been presented in Fig. 1 with Fermi level taken as an energy reference. One can observe the followings trends: (1) Before the arrival of any gas molecule, the band structures of C₂N:Mn show great discrepancy between spin-up and spin down as shown in Fig. 2(a). Single-atom catalyst Mn introduces a large magnetization in the lattice of about $M = 4.868 \mu_B$. (2) Case of N₂ physisorption: Fig. 2(g) shows the mimic effects of weak interaction of N₂ with C₂N:Mn on the band structure. Basically, one can notice the introduction of two discrete states (i.e., one localized state at energy $E \approx -0.4$ eV in the spin-up bands and another one at energy $E = -0.75$ eV in the spin-down bands); which should be attributed to the non-bonding states of the molecular orbital of N₂ molecule. (3) Strongly chemisorbed molecules (CO, CO₂ and O₂): These three molecules exhibit strong chemisorption processes with C₂N:Mn as was evidenced by the large charge transfers shown in Table-1 and was explained in details in sub-Sect. 3a in discussing results of Figure-1. Their corresponding band structures (see Panels 2b, 2c and 2 h, respectively) show the evidence of enormous changes to occur in the spin-down band structures. For more details, one must deal with density-of-states perspectives (e.g., see next sub-sections). Nevertheless, these modifications happening in the spin-down band-structures might be originated from the huge reductions in magnetization (see Table-1) of values $\Delta M = -0.303 \mu_B$, $-0.913 \mu_B$ and $-1.011 \mu_B$, respectively. (4) Weakly chemisorbed molecules (H₂O, H₂S, H₂): Their corresponding band-structures (see Panels 2e, 2f, and 2d, respectively) show less affected bands than those of the previous group of molecules. Basically, one can notice some localized states at energies $E \approx -0.85$ eV and $E \approx -1.2$ eV introduced in the spin-up bands by H₂O and H₂S molecules, respectively. Besides these effects, small changes might be introduced by all these molecules (H₂O, H₂S, and H₂) in the spin-down bands. Consequently, the effects of these molecules interacting with the C₂N:Mn lattice on the magnetization are mimic of order $+0.081 \mu_B$, $+0.099 \mu_B$ and $-0.035 \mu_B$, respectively.

Spin-polarized density of states. Figure 3 displays the spin-polarized total density of states (TDOS) for the same systems studied in Fig. 2. The spin-up (down) bands are shown in blue (red) color. The Fermi energy is taken as an energy reference ($E_F = 0$). The common trend between all panels is that they all show not only metallic behavior but also the existence of magnetization, as revealed by the existence of the discrepancy between TDOS of spin-up and TDOS of spin down in each single panel. The value of magnetization in units of Bohr magneton (μ_B) is displayed in each panel. The difference of magnetization is defined as $\Delta M = M_g - M_0$, where M_g and M_0 are total magnetization with and without gas molecule, respectively. The starting magnetization of the substrate (i.e., corresponding to C₂N:Mn without gas) is calculated to be $M_0 = 4.868 \mu_B$. The discrepancy between two TDOSs of spin-up and spin-down should be proportional to the magnitude of magnetization. By taking C₂N:Mn without gas molecule as a reference of magnetization, then ΔM should be a measure of the variation of that discrepancy. Figure 3 does corroborate the results of magnetization in measuring the effect of adsorption on the electronic structure in case of existence of magnetic dopant such as our Mn-catalyst. So, one can categorize three groups: (1) Case of physisorption (N₂ molecule): This adsorption has the least effect as revealed by the small decrease in magnetization $\Delta M = -0.027 \mu_B$. (2) Strongly chemisorbed molecules (CO, CO₂, O₂): These adsorptions have the largest effects on both electronic structure and magnetization. The variation of magnetization recorded to be $\Delta M = -0.303 \mu_B$, $-0.913 \mu_B$, and $-1.011 \mu_B$, respectively. (3) Weakly adsorbed molecules (H₂O, H₂S, H₂): Here the magnetization varies within few hundredths of Bohr magneton (i.e., $-0.035 \mu_B$, $+0.081 \mu_B$, and $+0.099 \mu_B$, respectively). In order to further investigate the origin of the discrepancy (i.e., ΔM), one needs to dig into the spin-polarized partial and orbital density of states that we do next.

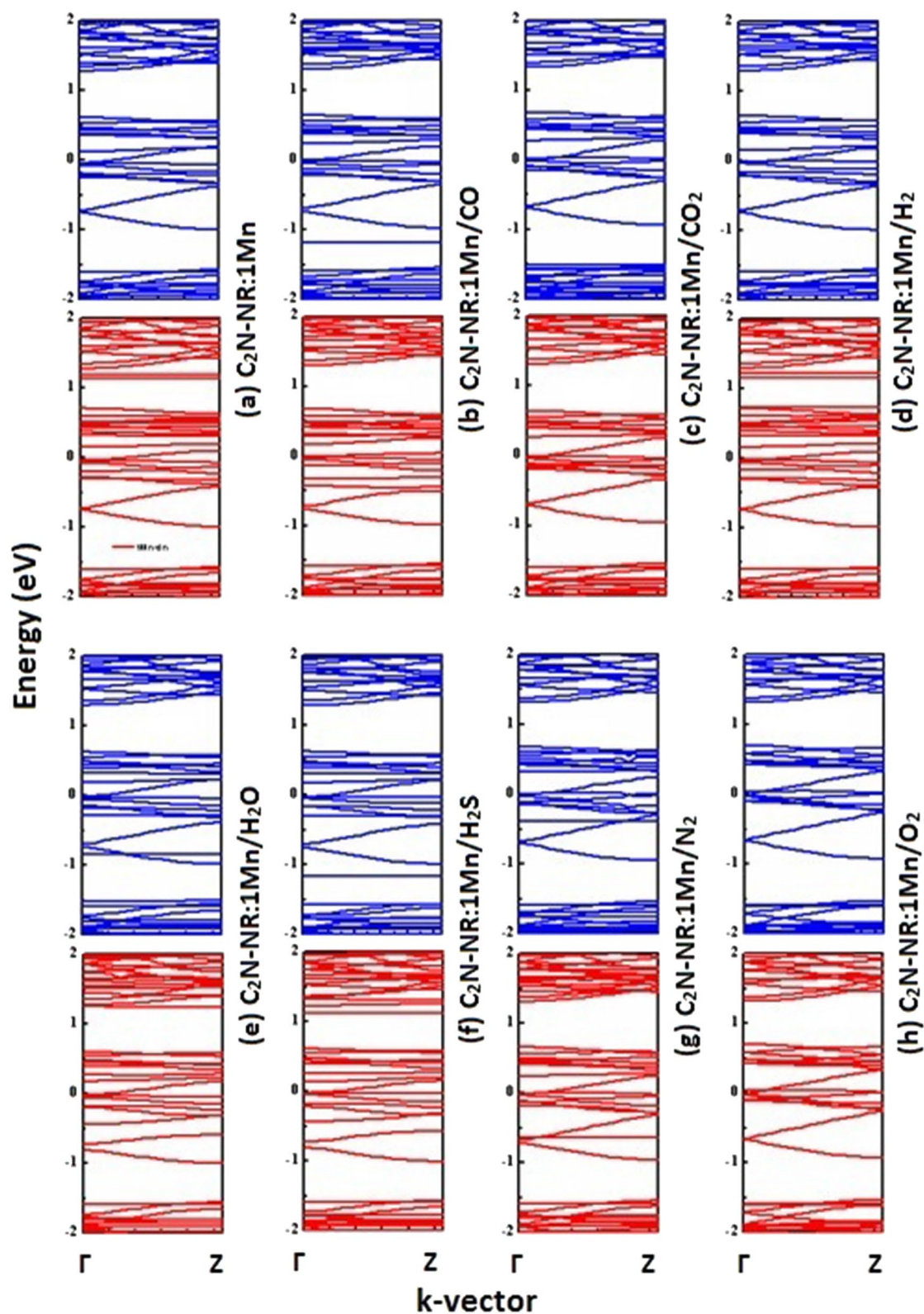


Figure 2. Electronic band structures of $C_2N-NR:1Mn$ after adsorption of various gas molecules. Spin-up (down) bands are shown by blue (red) color.

Magnetization effects. To inspect the effects of magnetization of Mn-catalyst when embedded into the pore of C_2N-NR , one needs to carry on further calculations such as the spin-polarized partial density of states

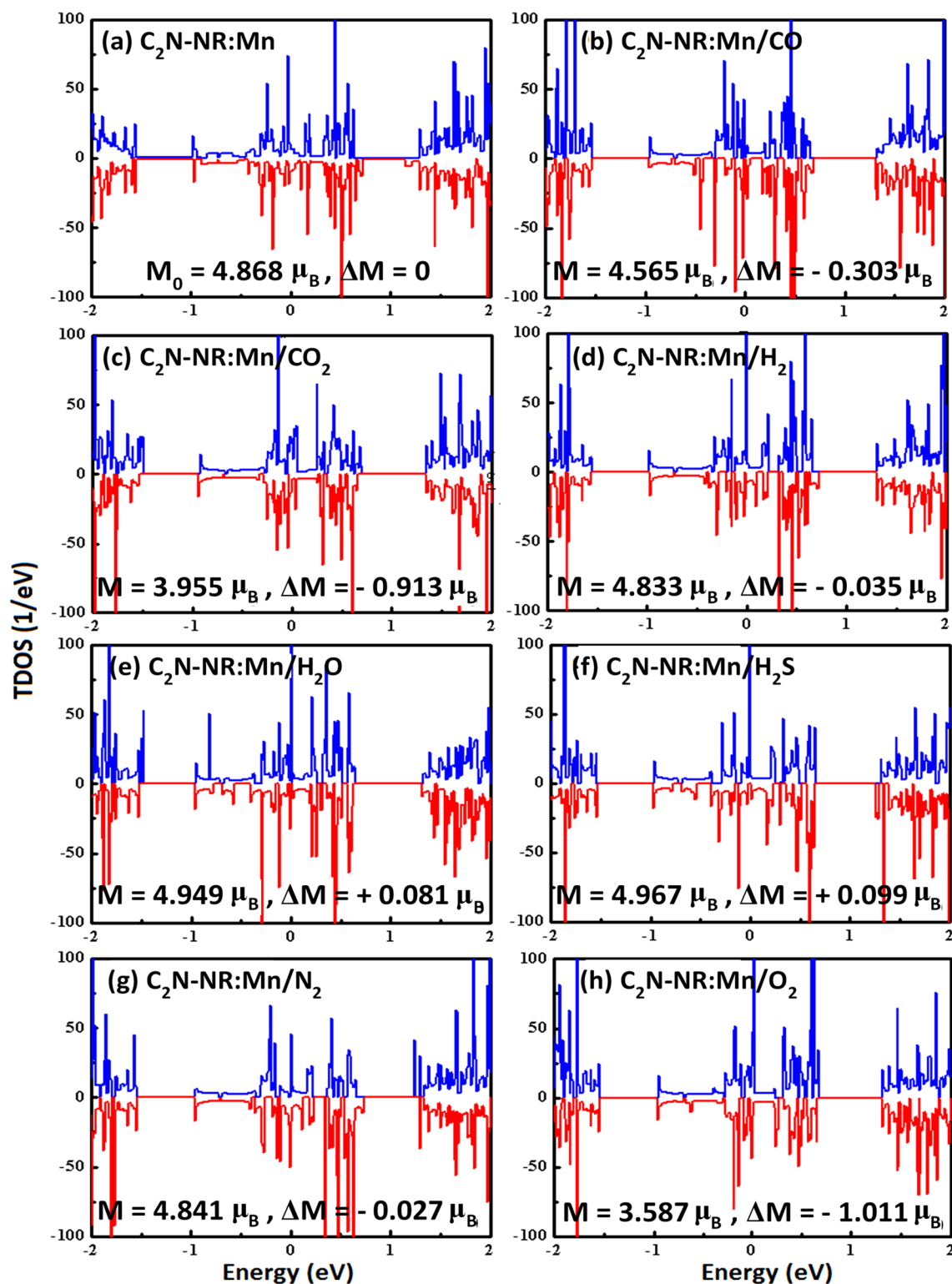


Figure 3. Spin-polarized Total Density of States (TDOS) for C_2N -NR:1Mn with various gas molecules.

(PDOS) and orbital density of states (ODOS). Figure 4 displays the results of spin-polarized PDOS on same systems presented in previous figure. In each panel, spin-up and spin-down contributions to PDOS are presented on the positive and negative sides, respectively. Moreover, the PDOS are clearly shown to have many peaks which correspond to Van-Hove singularities as characteristics of DOS of 1D systems. It is worth eliciting that in all panels hydrogen contributions should be expected as the hydrogen atoms were used to saturate the dangling bonds at the NR-edges. It is further clearly noticed the existence of asymmetry between spin-up and spin-down

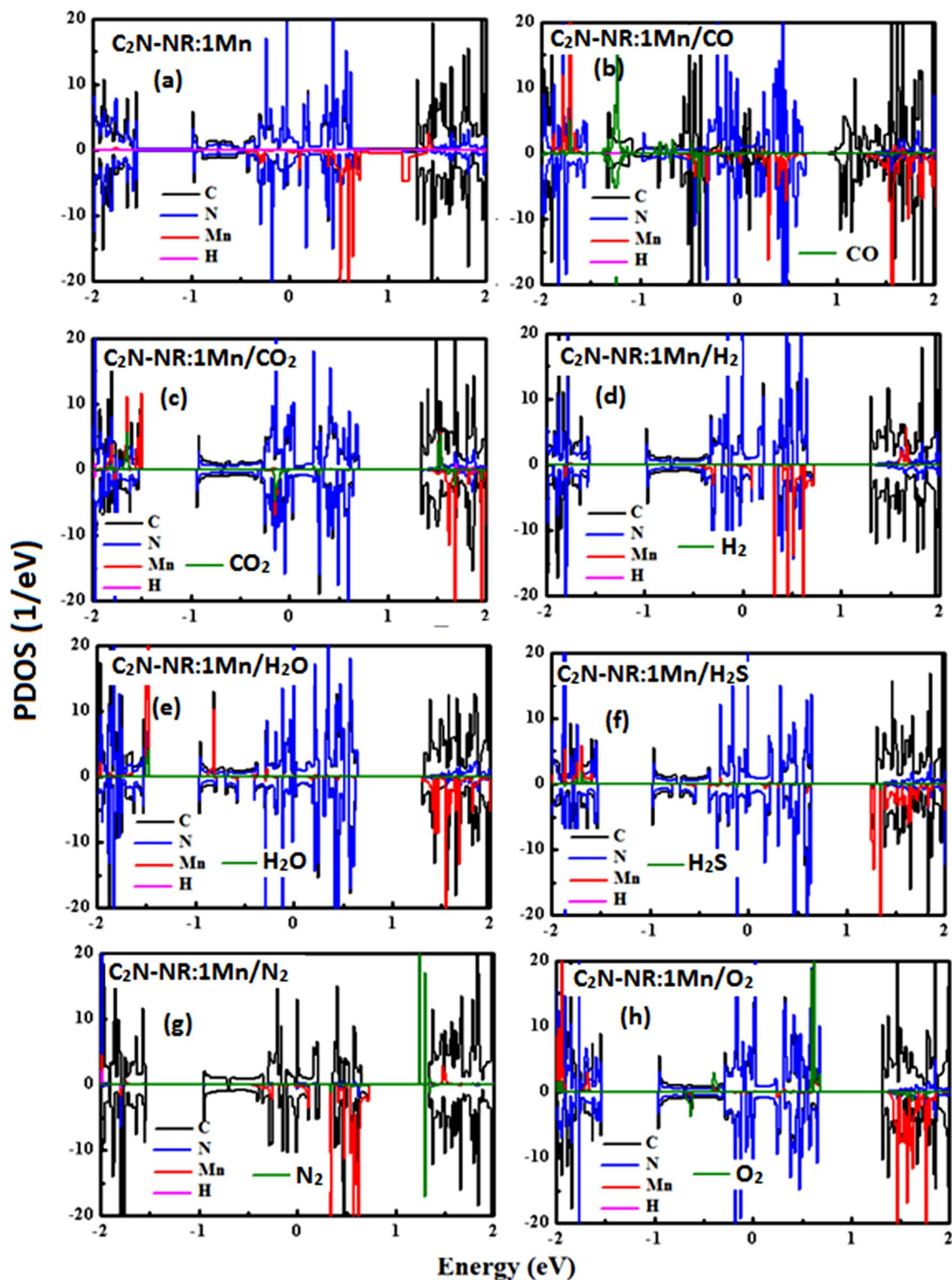


Figure 4. Spin-polarized Partial density of States (PDOS) for $C_2N-NR:Mn$ with various gas molecules.

contributions whose discrepancy should account for the formation of magnetization. First, one should start describing the case of the substrate or the platform to be used for the gas detection or sensing.

Panel 4(a) shows the case of $C_2N-NR:Mn$ before the arrival of any gas molecule. Mn-catalyst's PDOS (in red color) is shown to have clearly huge asymmetry with large contribution from spin-down states. Mn is located at the pore center and that should be considered to be the center of the magnetization. Mn-catalyst would induce some magnetization to neighboring atoms (i.e., so called "spin relaxation"). So, N-atoms' PDOS (blue color), in turn, shows some asymmetry to reveal its participation to the collective magnetization. C-atoms' PDOS (in black

color) is the least affected but does show some asymmetry in its overall profile especially above Fermi level. Now, one should discuss the effects of interactions of lattice (platform) with various gas molecules. In panel 4(b): CO molecule's PDOS (in green color) show great asymmetry contributions between spin-up and spin-down states. Near Fermi level, one can notice more contribution from spin-up states in response to the bonding of C-atom to Mn-catalyst due to the occurrence of chemisorption. So, one should expect some reduction of magnetization (i.e., $\Delta M = -0.303 \mu_B$). In panels 4(c,h): CO₂ and O₂ molecules' PDOSs (in green color) show even stronger effect than CO-molecule. Large contribution is due to spin-up states and causing large reductions in magnetization (i.e., $\Delta M = -0.913 \mu_B$ and $-1.011 \mu_B$, respectively). In panels 4(d,e,f): H₂, H₂O and H₂S molecules' PDOSs (in green color) are basically overlapped to follow the lattice profile. So, the asymmetry is not pronounced as in previous case and consequently the effect on magnetization is mimic (i.e., $|\Delta M| = 0.03-0.09 \mu_B$). The last panel to discuss is panel 4(g): N₂ molecule exhibits physisorption process so that its PDOS shows discrete molecular levels (i.e., see 2 spin-up states at energies $E = +1.2$ eV and $+1.3$ eV, and one spin-down state at energy $E = +1.3$ eV). Yet somehow, small magnetic moment got induced into the N₂ molecule by its being close above Mn-catalyst at a distance of about 3.32 Å (i.e., with $\Delta M = -0.027 \mu_B$).

Figure 5 shows the results of ODOS on the same systems studied in previous figure. This figure should investigate the original atomic orbital contributing to magnetization or causing effect on it. Panel 5(a) shows the case of our substrate/platform (i.e., C₂N-NR:Mn). The valence electrons in Mn-catalyst reside at s and d-states. Panel 5(a) shows that d-states have huge contribution to magnetization by having huge discrepancy between spin-up and spin-down ODOs. N and C atoms are forming the lattice with planar hybridization sp² while their P_z-orbitals populate the states at Fermi level and are accessible to be perturbed under the effect of magnetization; especially if this latter is attributed to z-based d-orbitals (i.e., d_{yz} , d_{zx} , d_{z^2}). So, we decided to present only P-orbitals of C, N, S and O atoms to assess their contributions to magnetization (with PDOS in light-blue color). Panels 5(b,c,h) show the cases of strong chemisorption processes with CO, CO₂ and O₂ molecules. It seems that the formation of an axial σ -bond between the molecule and Mn-catalyst would impose on the molecule to get its electronic contributions from spin-up states because Mn-catalyst has mostly spin-down states near Fermi level. This is to fulfill the requirements of Pauli-exclusion principle. In doing such act and having strong covalent bond would reduce the discrepancy in electronic population between spin-up and spin-down. Consequently, such Pauli exclusion principle effect would cause large reductions in magnetization. Panels 5(d,e,f) correspond to the weak chemisorption processes of H₂, H₂O and H₂S molecules, respectively. The chemical bonds here are weaker and Pauli-exclusion principle is less effective. So, the discrepancy between spin-down and spin-up PDOSs are less pronounced than those of the previous group of molecules. So, these latter chemisorption processes cause less effect on magnetization. Last case is in Panel 5(g) corresponding to the physisorption of N₂ molecule. The molecular states are discrete and having less discrepancy between spin-up and spin-down states. So, the effect on magnetization is the least one.

Charge transfer. Figure 6 displays the difference in charge density plot between the cases after the adsorption and before the adsorption for 7 molecules adsorbed on C₂N-NR:Mn substrate in the following order: (a) CO, (b) CO₂, (c) H₂, (d) H₂O, (e) H₂S, (f) O₂, and (g) N₂ molecules. To study the charge-transfer process between molecule and substrate/platform, it is customary to explore one of three methods: (i) Compare the charge contour plots before and after adsorption; or (ii) Compare the plots of the highest occupied molecular orbital (HOMO) and the lowest unoccupied molecular orbital (LUMO) before and after adsorption; or (iii) Do everything in one plot illustrating the charge difference/transfer such as the one shown in Fig. 6, where yellow (cyan) color indicates charge depletion (accumulation).

In all cases, the 7 molecules are oxidizing the Mn-catalyst. In the 6 cases of chemisorption, the molecule is attached to Mn-catalyst via covalent bond with partial ionic character. Panels 6 (a,b) show that the cases of chemisorption of CO and CO₂ molecules to be associated with the depletion of charge from vicinity of Mn and its shifting toward C and O in the molecule as well as the 6 N atoms neighboring Mn. The discrepancy in electronegativity characters between the atoms play a major role in the charge distribution along the bond. For instance, $\chi^O = 3.44 > \chi^N = 3.04 > \chi^C = 2.55 > \chi^{Mn} = 1.55$ (in units of Pauling) can be used to justify the accumulation of charge at the sites of anion atoms of higher electronegativity. Panel 6(c) shows the case of chemisorption of H₂ to be accompanied with the transfer of charge toward H atoms because $\chi^H = 2.20 > \chi^{Mn} = 1.55$ (in Pauling units). Furthermore, the charge distribution clearly shows the H-atoms to be well separated confirming the occurrence of chemisorption associated with a weak molecular dissociation. Panels 6(d,e) show that the H₂O and H₂S molecule maintain their molecular structures while the anion atom is making somehow weak covalent bonding with Mn-catalyst (i.e., so less ΔM occurs). Panel 6(f) demonstrates a kind of strong chemisorption with O₂ molecule with strong charge transfer to it. Last panel 6(g) shows the case of N₂ physisorption. It is clearly shown almost inexistence of charge transfer between molecule and substrate.

Figure 7 summarizes our findings and displays the results of Table-1 concerning the absolute values of adsorption energy, charge transfer, and change in magnetization. Clearly, one can distinguish two groups of molecules in the perspective of their interactions with the SAC-Mn embedded in C₂N-NR: (i) A first group with strong and well-pronounced oxidizing character (e.g., CO, CO₂ and O₂) with strong chemisorption: These molecules have strong adsorption energy. They make strong covalent bonds with SAC-Mn and thus introduce spin-up states to TDOS in the Fermi-energy region and consequently reduce the discrepancy between spin-up and spin-down TDOS. Thus, they are able to reduce enormously the net magnetization. (ii) A second group with vanishing oxidation or rather known to have reducing character (e.g., N₂, H₂, H₂O, and H₂S) with either physisorption or weak chemisorption: These molecules have weak interactions with SAC-Mn. Thus, they contribute mostly with spin-down states to TDOS in the Fermi-energy region of same kind as the magnetic Mn-atom. So, the discrepancy between spin-up and spin-down TDOS remains about unchanged and the effect on changing the

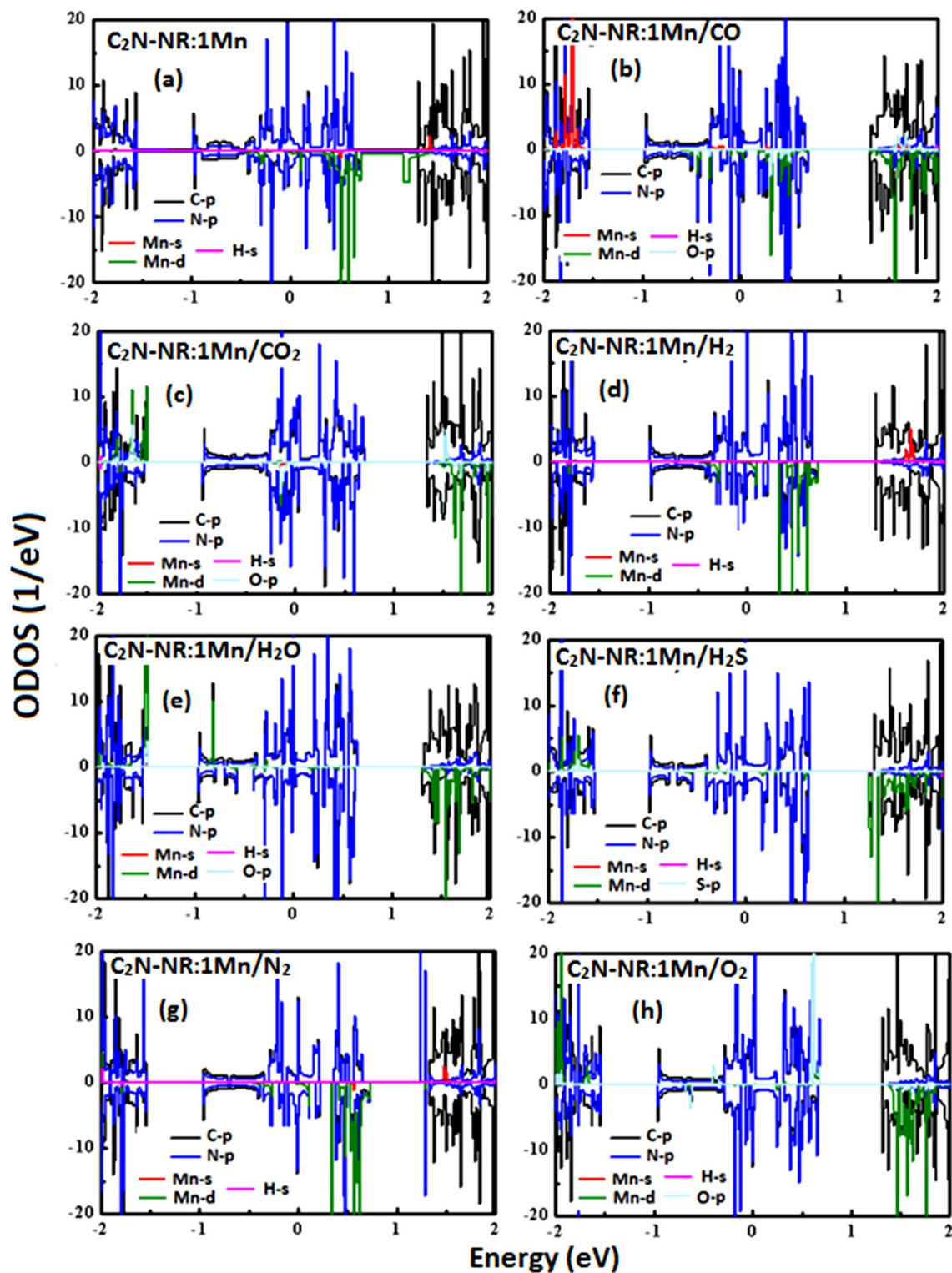


Figure 5. Spin-polarized Orbital density of states (ODOS) for $C_2N-NR:Mn$ with various gas molecules.

magnetization would be vanishingly small (i.e., the magnetization is maintained robust or conserved). So, one can conclude that $C_2N:Mn$ would be a good candidate for platform in the fabrication of magnetic sensor with promising selectivity to detect the oxidizing gas molecules (CO , CO_2 and O_2).

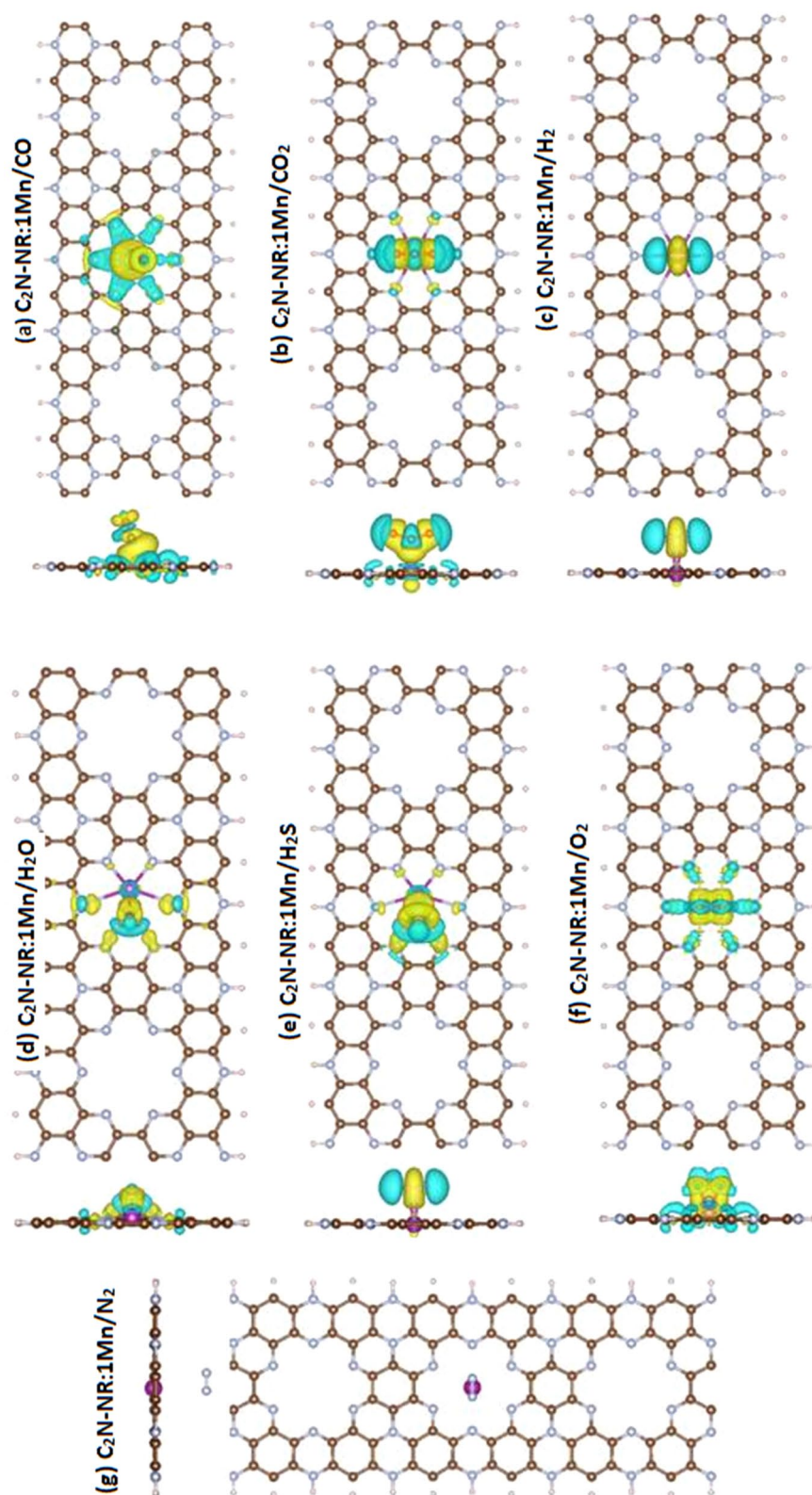


Figure 6. Charge-difference density plots for $C_2N-NR:1Mn$ with various gas molecules. Yellow (cyan) color indicates charge depletion (accumulation).

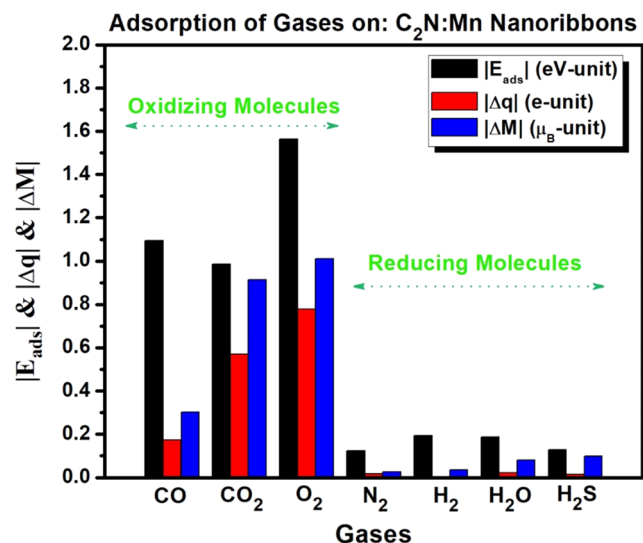


Figure 7. Comparison of absolute values of adsorption energy ($|E_{ads}|$), charge transfer ($|\Delta q|$) and variation of magnetization ($|\Delta M|$) from before to after the adsorption of gas molecules.

Conclusions

Aiming for Gas-sensing selectivity, we presented a theoretical study of functionalized C_2N nanoribbons based on the DFT-package of VASP. Magnetic atom such as Mn is used as SAC embedded in C_2N pore to test the effect on the adsorption properties of various gases of interest in energy and environmental sciences (e.g., CO, CO₂, H₂, H₂O, H₂S, N₂ and O₂). The results of atomic relaxations show that pristine C_2N -NR always alters physisorption processes with these gases while C_2N -NR:Mn has the full ability to alter chemisorption processes with all gas molecules except N₂. The results of molecular chemisorption can be categorized into two groups:

- Strong chemisorption with oxidizing CO, CO₂, and O₂ gas molecules is evidenced by large binding energy and charge transfer. Mn-catalyst seems very active in interacting with the oxidizing gas molecules. Furthermore, SAC-Mn induces large magnetization into the system by contributing enormously with spin-down states to the electronic band-structure at Fermi-energy region, while its interaction with these mentioned molecules would introduce spin-up states at Fermi level to compromise and rather reduce the magnetization. Actually, such phenomenon occurs as a consequence of the Pauli-exclusion principle;
- Weak chemisorption with reducing H₂, H₂O, and H₂S gas molecules is observed with low binding energy and charge transfer. The interaction does not affect the asymmetry in spin-up and spin-down statistics and the discrepancy remains about the same between the states of spin-up and spin-down. Consequently, these adsorptions have mimic effects on magnetization (i.e., M persists to remain constant).

The results suggest that C_2N -NR:Mn is a promising platform for gas sensing of oxidizing CO, CO₂ and O₂ gas molecules with high sensitivity and selectivity. The efficiency of the sensor could be further enhanced if it is combined with magnetic sensor to detect the change in magnetization and the system would be of great importance in environmental applications.

Computational methodology. Density functional theory (DFT) has been well established to be the most reliable to predict the ground state properties of materials, including the adsorption properties. Perhaps, the worldwide most popular and reliable package is the Vienna Ab-initio Simulation Package (VASP)⁴¹, which masters to incorporate all basic interactions, such as spin-polarization, magnetic (Hubbard U) and dipole-dipole long-range (i.e., van der Waals) interactions. Furthermore, the package is competent to deal with challenges in our system which involves magnetic dopants (e.g., manganese “Mn”) and its binding as embedded in pore of C_2N as well as its interaction with gas molecules in order to reliably predict the occurrence of either physisorption or chemisorption. Our calculations include atomic relaxation to study the adsorption of various gas molecules, known to be either oxidizing (e.g., CO, CO₂, O₂) or reducing (e.g., H₂, H₂O, H₂O, N₂), spin-polarized band structures and partial as well as orbital densities of states, difference of charge density plots, Bader-charge analysis, and magnetic moments. Targeting to use such system of Mn-embedded in C_2N as a platform of electrical gas sensor, we decided to study the system in the nanoribbon form⁴⁰.

As a model, we have designed a nanoribbon shape with zigzag edges and made the dangling bonds be saturated at the two edges by bonding them with hydrogen atoms. Actually, such a structure was used before us and exists in literature^{40,41}. We made sure that it is thermodynamically stable and it yields metallic behavior (i.e., $E_g = 0$), to make it suitable for gas-sensing applications. The designed C_2N -NR structures are displayed in Figure-1. We emphasize that the primitive cell of pristine C_2N -NR is composed of 50 atoms (i.e., 32 C + 10 N + 8

Spin Configuration	E_{TOT} (eV)	M_{TOT} (μ_B)	M/Mn-atom: Mn ₁ , Mn ₂ (μ_B)	Mn–Mn Distance	Favored Coupling
FM	–1210.504	7.010	3.099, 3.101	2.207	No
AFM	–1211.099	0.000	3.458, –3.458	2.178	Yes

Table 2. Total energy and magnetization and separate magnetic moments of Mn dimer embedded in C₂N. Two spin configurations (FM and AFM) were tested.

H atoms). The supercell is composed of 3 primitive cells so the total number of atoms is 150 atoms (i.e., 96 C + 30 N + 24 H atoms). Thus, in summary, our supercell would contain 1D nanoribbon having a periodicity along x-axis with length $L = 29.51 \text{ \AA}$ and a width of approximately about $W \approx 12 \text{ \AA}$, and 3 pores each of size/diameter of about 5.68 \AA . Given the size of the C₂N-NR, our computational supercell was set to the dimensions (A,B,C) = (29.51, 22, 12) \AA units. The B and C dimensions are large enough to ensure the isolation of C₂N-NR with its mirror symmetries along y and z directions, respectively. Throughout our present investigation, we used as adsorbent either (1) Pristine C₂N-NR, or (2) SAC-Mn embedded in the central pore of C₂N-NR; and as adsorbate one gas molecule at a time among the 7 gases mentioned above.

As a method, the calculation employs plane-wave basis set (with cutoff energy of 500 eV). Within the framework of the projected-augmented plane-waves (PAW) method, the electronic exchange–correlation was treated using the generalized gradient approximation (GGA + U)⁴³, where + U stands for the Hubbard parameter which is usually added in case of highly-correlated spin systems such as transition metal, and especially those which are ferromagnetic such as in our case “Mn”. The Hubbard parameter $U = 3.5 \text{ eV}$ was taken for Mn 3d-states was due to reference 43. Furthermore, we included in our calculations DFT-D3 technique^{44,45} to take care of the van der Waals interactions, which are important in the study of adsorption. In the geometry optimization, all the atoms in the supercell were allowed to relax until the Hellmann–Feynman force on each atom became smaller than 0.01 eV \AA^{-1} ; whereas the tolerance for the total energy convergence was set to 10^{-4} eV . The sampling of the Brillouin zone was performed using $25 \times 1 \times 1$ Monkhorst–Pack technique⁴⁶ for total energy calculations. However, the density of states’ calculations were performed with a relatively denser grid of $50 \times 1 \times 1$ k-mesh. The adsorption energy of any gas molecule on C₂N-NR substrate was evaluated using the formula:

$$E_{\text{ads}} = E_{\text{C}_2\text{N-NR}+\text{gas}} - E_{\text{C}_2\text{N-NR}} - E_{\text{gas}}, \quad (1)$$

where $E_{\text{C}_2\text{N-NR}+\text{gas}}$, $E_{\text{C}_2\text{N-NR}}$, and E_{gas} are the total energies of the system of pristine (or Mn-embedded) C₂N-NR with and without gas molecule and the gas molecule, respectively. Furthermore, we emphasize that the charge transfer was estimated using the Bader-charge analysis⁴⁷.

In order to address the magnetic coupling, and to find the most stable magnetic state, a dimer of Mn is embedded in the pore of C₂N-NR (i.e., C₂N-NR:2Mn) and the system is relaxed under ferromagnetic (FM) and anti-ferromagnetic (AFM) spin configurations. The obtained results of total energy and magnetization are summarized in Table 2.

The results were in favor of anti-ferromagnetic state as having lower total energy by $\Delta E = E_{\text{tot}}(\text{FM}) - E_{\text{tot}}(\text{AFM}) = +0.595 \text{ eV}$ value. Nevertheless, in our present investigation, the focus will not be upon the dimer-atom-catalyst (DAC) case but the full focus will be upon the single-atom-catalyst (SAC) case. So, we study single Mn atom embedded in C₂N-NR and assess its interaction with various gas molecules. Definitely, we expect non-zero magnetic moment and rather large effect of magnetization on the electronic structures as will be demonstrated by the spin-relaxation effects.

Received: 1 April 2021; Accepted: 21 July 2021

Published online: 04 August 2021

References

- Novoselov, K. S. *et al.* Electric field effect in atomically thin carbon films. *Science* **306**(5696), 666–669 (2004).
- Geim, A. K. & Novoselov, K. S. The rise of graphene. *Nat. Mater.* **6**(3), 183–191 (2007).
- Schedin, F. *et al.* Detection of individual gas molecules adsorbed on graphene. *Nat. Mater.* **6**(9), 652–655 (2007).
- Varghese, S. S., Lonkar, S., Singh, K. K., Swaminathan, S. & Abdala, A. Recent advances in graphene based gas sensors. *Sens. Actuat. B* **218**, 160–183 (2015).
- Rumyantsev, S., Liu, G., Shur, M. S., Potyraiilo, R. A. & Blandin, A. A. Selective gas sensing with single pristine graphene transistor. *Nano Lett.* **12**(5), 2294–2298 (2012).
- Schwierz, F. Graphene transistors. *Nat. Nanotechnol.* **5**(7), 487–496 (2010).
- Liao, L. *et al.* High-speed graphene transistors with a self-aligned nanowire gate. *Nature* **467**(7313), 305–308 (2010).
- Bonaccorso, F., Sun, Z., Hasan, T. & Ferrari, A. C. Graphene photonics and optoelectronics. *Nat. Photon.* **4**(9), 611–622 (2010).
- Wang, X., Zhi, L. & Mullen, K. Transparent, conductive graphene electrodes for dye-sensitized solar cells. *Nano Lett.* **8**(1), 323–327 (2008).
- Son, D. I. *et al.* Emissive ZnO-graphene quantum dots for white-light-emitting diodes. *Nat. Nanotechnol.* **7**(7), 465–471 (2012).
- Vlasov, A. I., Terent’ev, D. S. & Shakhnov, V. A. Graphene flexible touchscreen with integrated analog-digital converter. *Russian Microelectronics* **46**(3) 192–199 (2017).
- Mueller, T., Xia, F. & Avouris, P. Graphene photodetectors for high-speed optical communications. *Nat. Photonics* **4**(5), 297–301 (2010).
- Sun, Z. *et al.* Graphene mode-locked ultrafast laser. *ACS Nano* **4**(2), 803–810 (2010).
- Han, W., Kawakami, R. K., Gmitra, M. & Fabian, J. Graphene spintronics. *Nat. Nanotechnol.* **9**(10), 794–807 (2014).
- Yazyev, O. V. & Katsnelson, M. I. Magnetic correlations at graphene edges: Basis for novel spintronics devices. *Phys. Rev. Lett.* **100**(4), 047209 (2008).

16. Feng, L. & Liu, Z. Graphene in biomedicine: opportunities and challenges. *Nanomedicine* **6**(2), 317–324 (2011).
17. Yang, Y., Asiri, A., Tang, Z., Du, D. & Lin, Y. Graphene based materials for biomedical applications. *Mater. Today* **16**(10), 365–373 (2013).
18. Bae, S. H. *et al.* Graphene-based transparent strain sensor. *Carbon* **51**(1), 236–242 (2013).
19. Wang, T., Ouyang, Z., Wang, F. & Liu, Y. A review on graphene strain sensors based on fiber assemblies. *SN Appl. Sci.* **2**(5), 862 (2020).
20. Mahmood, J. *et al.* Nitrogenated holey two-dimensional structures. *Nat. Commun.* **6**(1), 6486 (2015).
21. Xu, J. *et al.* 2D frameworks of C₂N and C₃N as new anode materials for lithium batteries. *Adv. Mater.* **29**(34), 1702007 (2017).
22. Huang, C., Mahmood, J., Wei, Z., Wang, D., Liu, S., Zhao, Y., Noh, H.J., Ma, J., Xu, J. & Baek, J.B. Metal (M = Ru, Pd and Co) embedded in C₂N with enhanced lithium storage properties. *Materials Total Energy* **14**(11) 100359 (2019).
23. Wu, D., Yang, B., Chen, H. & Ruckenstein, E. Nitrogenated holey graphene C₂N monolayer anodes for lithium- and sodium-ion batteries with high performance. *Energy Storage Mater.* **16**(1), 574–580 (2019).
24. Lokhande, A. C., Qattan, I. A., Lokhande, C. D. & Patole, S. P. Holey graphene: an emerging versatile material. *J. Mater. Chem. A* **8**(3), 918–977 (2020).
25. Wu, D., Yang, B., Ruckenstein, E. & Chen, H. Functionalization: an efficient approach to open and close channels for electron transfer in nitrogenated holey graphene C₂N anodes in sodium-ion batteries. *J. Phys. Chem. Lett.* **10**(4), 721–726 (2019).
26. Liang, S., Hao, C. & Shi, Y. The power of single-atom catalysis. *Chem. Cat. Chem.* **7**(17), 2559–2567 (2015).
27. Liu, J. Catalysis by supported single-metal atoms. *ACS Catal.* **7**(1), 34–59 (2017).
28. Shen, Z. *et al.* 3d transitional-metal single atom catalysis toward hydrogen evolution reaction on MXenes supports. *Int. J. Hydrogen Energy* **45**(28), 14396–14406 (2020).
29. He, B. L., Shen, J. S. & Tian, Z. X. Iron-embedded C₂N monolayer: a promising low-cost and high-activity single-atom catalyst for CO oxidation. *Phys. Chem. Chem. Phys.* **18**(35), 24261–24269 (2016).
30. Cui, X. *et al.* C₂N-graphene supported single-atom catalysts for CO₂ electrochemical reduction reaction: mechanistic insight and catalyst screening. *Nanoscale* **10**(32), 15262–15272 (2018).
31. Gao, Z., Yang, W., Ding, X., Lv, G. & Yan, W. Support effects in single-atom iron catalysts on adsorption characteristics of toxic gases (NO₂, NH₃, SO₃ and H₂S). *Appl. Surf. Sci.* **436**(32), 585–595 (2018).
32. Lin, S., Qiao, Q., Chen, X., Hu, R. & Lai, N. Transition metal atom doped C₂N as catalyst for the oxygen reduction reaction: a density functional theory study. *Int. J. Hydrogen Energy* **45**(51), 27202–27209 (2020).
33. Guerrero-Aviles, R. & Orellana, W. Hydrogen storage on cation-decorated biphenylene carbon and nitrogenated holey graphene. *Int. J. Hydrogen Energy* **43**(51), 22966–22975 (2018).
34. Banu, A. A., Karazhanov, S. Z., Kumar, K. V. & Jose, S. P. Platinum doped iron carbide for hydrogen evolution reaction: The effects of charge transfer and magnetic moment by first-principle approach. *Int. J. Hydrogen Energy* **45**(56), 31825–31840 (2020).
35. Zhao, J., Zhao, J. X., Li, F. & Chen, Z. Copper dimer supported on a C₂N layer as an efficient electro-catalyst for CO₂ reduction reaction: a computational study. *J. Phys. Chem. C* **122**(34), 19712–19721 (2018).
36. Ma, D. W. *et al.* 3d transition metal embedded C₂N monolayers as promising single-atom catalysts: a first-principles study. *Carbon* **105**(35), 463–473 (2016).
37. Liu, K. *et al.* Mn- and N-doped carbon as promising catalysts for oxygen reduction reaction: theoretical prediction and experimental validation. *Appl. Catal. B Environ.* **243**, 195–203 (2019).
38. Impeng, S. *et al.* A MnN₄ moiety embedded graphene as a magnetic gas sensor for CO detection: a first principles study. *Appl. Surf. Sci.* **473**, 820–827 (2019).
39. Du, J., Xia, C., Xiong, W. & Zhao, X. Tuning the electronic structures and magnetism of two-dimensional porous C₂N: Via transition metal embedding. *Phys. Chem. Chem. Phys.* **18**(32), 22678–22686 (2016).
40. Wang, Y. *et al.* Tunable electronic structure and magnetic moment in C₂N nanoribbons with different edge functionalization atoms. *Phys. Chem. Chem. Phys.* **19**(23), 15021–15029 (2017).
41. Hafner, J. Ab-initio simulations of materials using VASP: density-functional theory and beyond. *J. Comp. Chem.* **29**(13), 2044–2078 (2008).
42. Saraiva-Souza, A., Smeu, M., Filho, J. G. S., Girao, E. C. & Guo, H. Tuning the electronic and quantum transport properties of nitrogenated holey graphene nanoribbons. *J. Mater. Chem. C* **5**(45), 11856–11866 (2017).
43. Song, N. H., Wang, Y. S., Zhang, L. Y., Yang, Y. Y. & Jia, Y. Density functional theory study of tunable electronic and magnetic properties of monolayer BeO with intrinsic vacancy and transition metal substitutional doping. *J. Mag. Mag. Mater.* **468**, 252–258 (2018).
44. Ali, M. & Tit, N. Adsorption of NO and NO₂ molecules on defected-graphene and ozone-treated graphene: first-principles analysis. *Surf. Sci.* **684**, 28–36 (2019).
45. Grimme, S., Antony, J., Ehrlich, S. & Krieg, H. A consistent and accurate ab initio parametrization of density functional dispersion correction (DFT-D) for the 94 elements H-Pu. *J. Chem. Phys.* **132**(15) 154104 (2010).
46. Monkhorst, H. J. & Pack, J. D. Special points for Brillouin-zone integration. *Phys. Rev. B.* **13**(12), 5188–5192 (1976).
47. Bader, R. F. W., MacDougall, P. J. & Lau, C. D. H. Bonded and non-bonded charge concentrations and their relation to molecular geometry and reactivity. *J. Am. Chem. Soc.* **106**(6), 1594–1605 (1984).

Acknowledgements

The authors are indebted to Drs. Golibjon Berdiyrov and Muhammad Ali for fruitful discussions and the National Water and Energy Center (NWECC) at the UAE University for the financial support (under research grants #: 31R145 and 31R216).

Author contributions

M.M. performed VASP calculations and prepared most of the Figures. N.T. supervised the project and revised the Figures as well as wrote the manuscript. Thus their contributions can be divided as 60% and 40%, respectively.

Competing interests

The authors declare no competing interests.

Additional information

Correspondence and requests for materials should be addressed to N.T.

Reprints and permissions information is available at www.nature.com/reprints.

Publisher's note Springer Nature remains neutral with regard to jurisdictional claims in published maps and institutional affiliations.



Open Access This article is licensed under a Creative Commons Attribution 4.0 International License, which permits use, sharing, adaptation, distribution and reproduction in any medium or format, as long as you give appropriate credit to the original author(s) and the source, provide a link to the Creative Commons licence, and indicate if changes were made. The images or other third party material in this article are included in the article's Creative Commons licence, unless indicated otherwise in a credit line to the material. If material is not included in the article's Creative Commons licence and your intended use is not permitted by statutory regulation or exceeds the permitted use, you will need to obtain permission directly from the copyright holder. To view a copy of this licence, visit <http://creativecommons.org/licenses/by/4.0/>.

© The Author(s) 2021